

pubs.acs.org/NanoLett Letter

# Stretchable Thin-Film Transistors Based on Wrinkled Graphene and MoS<sub>2</sub> Heterostructures

Hyunchul Kim, He Lin Zhao, and Arend M. van der Zande\*



Cite This: https://doi.org/10.1021/acs.nanolett.3c05091



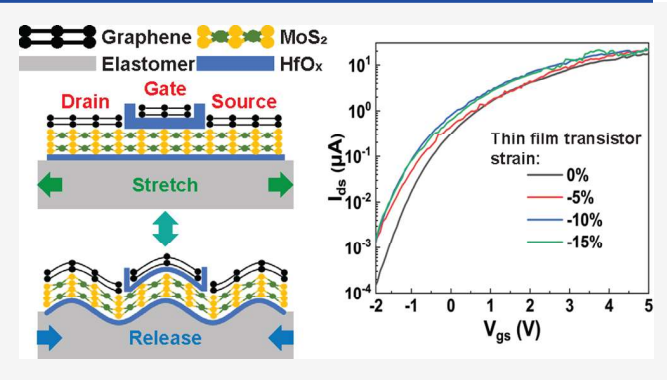
**ACCESS** I

Metrics & More

Article Recommendations

Supporting Information

**ABSTRACT:** Two-dimensional (2D) materials are outstanding candidates for stretchable electronics, but a significant challenge is their heterogeneous integration into stretchable geometries on soft substrates. Here, we demonstrate a strategy for stretchable thin film transistors (2D S-TFT) based on wrinkled heterostructures on elastomer substrates where 2D materials formed the gate, source, drain, and channel and characterized them with Raman spectroscopy and transport measurements. The 2D S-TFTs had initial mobility of  $4.9 \pm 0.7~{\rm cm^2/(V~s)}$ . The wrinkling reduced the strain transferred into the 2D materials by a factor of 50, allowing a substrate stretch of up to 23% that could be cycled thousands of times without electrical degradation. The stretch did not alter the mobility but did lead to strain-induced threshold voltage shifts by



 $\Delta V_{\rm T} = -1.9$  V. These 2D S-TFTs form the foundation for stretchable integrated circuits and enable investigations of the impact of heterogeneous strain on electron transport.

**KEYWORDS:** 2D materials, 2D heterstructures, stretchable electronics, transistors, buckling engineering

Stretchable thin film transistors (S-TFT) play a central role in the fields of wearable electronics, 1-3 artificial skins, 4,5 human/machine interfaces, 6-8 and soft robotics. 9,10 A major challenge is that typical semiconductor materials like intrinsically stretchable polymers and 3D deformable thin films pose a trade-off between electrical and mechanical performance. For instance, conventional thin-film materials, such as silicon, have high mobilities but are brittle, fracturing at 1.2% strain. 11 Conversely, intrinsically stretchable organic semiconductors have relatively low electrical mobilities of only 0.08–1.16 cm²/ (V s). 12

As atomically thin, covalently bonded crystals, two-dimensional (2D) materials have both excellent mechanical and electronic properties that break this typical trade-off.  $^{13,14}$  As a result, 2D materials are being actively explored for flexible and stretchable electronics.  $^{15,16}$  Currently, flexible electronics from 2D materials is more mature, with numerous device demonstrations such as controls for OLED arrays,  $^{17}$  image sensors,  $^{18}$  wearable healthcare devices,  $^{19}$  and flexible computational circuits.  $^{20,21}$  Flexible TFTs from 2D such as MoS $_2$  on elastomer substrates exhibit decent substrate dependent electrical mobilities ranging from 10.8 to 55 cm²/(V s) and on/off ratios spanning from  $10^4$  to  $10^{10}.^{20,22-24}$  However, flexible MoS $_2$  TFTs exhibit reliable operation only up to <2.1% of bending induced strain before structural failure.  $^{20,22-24}$ 

A current goal is to enable conformal and stretchable electronics by realizing stretchable transistors that take full advantage of the superlative electronic and mechanical

properties of 2D materials. Generally, stretchability is imparted through strategies like inducing 3D deformations like crumpling  $^{25-29}$  or wrinkling,  $^{30-32}$  as well as the application of kirigami, to create strategic cuts that enable thin films to bend, twist, and stretch. 33,34 Additionally, stretchability can also be facilitated by inducing interfacial slip. 35,36 These strategies take advantage of the intrinsic ultralow bending modulus of 2D materials as well as the low friction at the van der Waals interface to bring higher levels of 3D deformability without damaging the material 37,38 and have led to stretchable device demonstrations like deformable electrodes, 25 cell growth platforms, <sup>39</sup> electronic skin, <sup>40,41</sup> photodetectors, <sup>26,27,29</sup> and strain sensors. <sup>42</sup> The implementation of these strategies has significantly enhanced the strain resistance of 2D materialbased electrodes or phototransistors, achieving tolerances of up to 129% for slip,<sup>36</sup> more than 200% for crumpling,<sup>29</sup> and 200% for kirigami.<sup>33</sup> However, bringing these design concepts to more complex devices like transistors is challenging because they contain multiple active device layers, which should all have similar mechanical response. For example, integrating thin

Received: December 24, 2023 Revised: January 9, 2024 Accepted: January 10, 2024



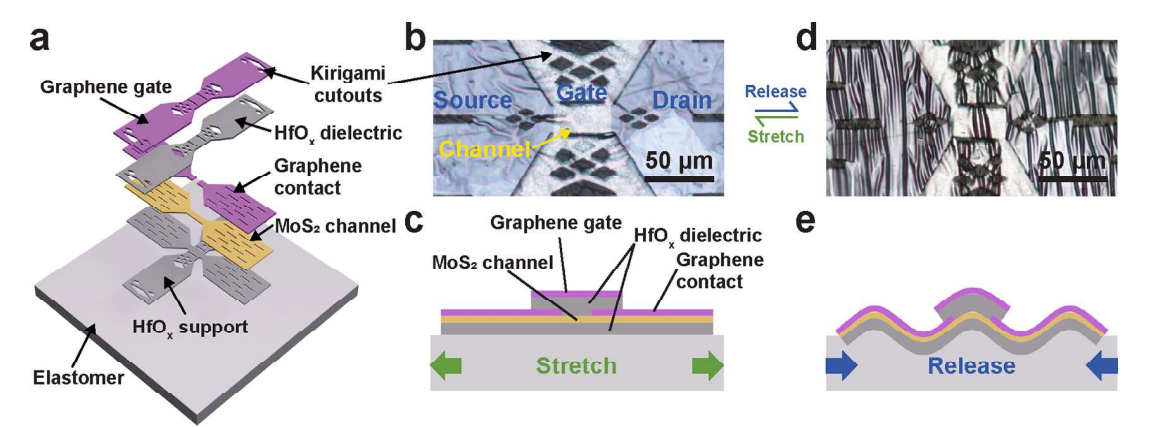


Figure 1. Structure of 2D S-TFT. (a) Schematic of all patterned device layers of the 2D S-TFT. (b) Optical image and (c) schematic cross section of the profile parallel to the channel of the initial flat 2D S-TFT on top of the prestretched substrate. (d) Optical image and (e) schematic cross section of the profile parallel to the channel of the 2D S-TFT after the prestretch has been released.

films of 3D materials such as gold electrodes with 2D components will lead to a mechanical and thickness mismatch, nullifying the benefits of the 2D materials.

Current studies have explored strategies including the application of ion-gel gates, <sup>43</sup> exfoliated h-BN as a dielectric layer with metallic electrodes, <sup>44</sup> and graphene as source/drain electrodes. <sup>45</sup> However, the achievable stretchability is still limited to a maximum of 14.2%, and many of these approaches are not scalable to independent arrays or circuits. The ideal solution to address the low fracture strain limit is the utilization of 2D materials for as many functional layers in the S-TFT as possible and incorporate design strategies for minimizing strain in 3D deformed structures.

Here, we propose a strategy for fabricating 2D heterostructure S-TFT (2D S-TFT) with an electronic performance comparable to 2D flexible electronics. We integrate 2D materials into multiple functional layers, with bilayer graphene as both the source/drain and gate electrodes and MoS<sub>2</sub> as the channel—the only non-2D layers being the HfO<sub>x</sub> dielectric and support layers. An improvement to this design that we considered but determined to be unfeasible would be to replace the HfO<sub>x</sub> with hexagonal boron nitride (hBN) which is well-known to improve the electrical mobility of 2D materials. However, currently, hBN may be synthesized via exfoliation or chemical vapor deposition, neither of which can simultaneously achieve the high quality, thickness, and size uniformity needed for this study. We impart stretchability by transferring the 2D s-TFT onto prestretched polymers and then releasing to induce wrinkling and incorporate kirigami cuts into the

Figure 1a is a schematic showing the layers of the 2D S-TFT. From top to bottom, the 2D S-TFT consists of a bilayer graphene top gate, a 16 nm thick HfO $_x$  gate dielectric layer, bilayer graphene source/drain contact electrodes, a monolayer or bilayer MoS $_2$  channel, an 11 nm thick HfO $_x$  mechanical support layer, and an elastomer substrate. We used slightly different designs to optimize for different measurements. For the Raman measurements, we used monolayer MoS $_2$  channels with length  $L=10~\mu{\rm m}$  and width  $W=10~\mu{\rm m}$ . For transport measurements, we used bilayer MoS $_2$  channels with length  $L=4~\mu{\rm m}$  and width  $W=30~\mu{\rm m}$ . All layers in the 2D S-TFT possess kirigami cutouts, adopting line-shaped or diamond-shaped patterns, which serve to enhance stretchability. The aim of incorporating bilayer graphene and MoS $_2$  into the design

was to enhance the conductivity, even in cases where the material experiences partial damage due to applied strain.  $^{46,47}$  See the Supporting Information and Figures S1 and S2 for the process details. Briefly, we prefabricated the 2D S-TFT on a sacrificial gold thin film on a SiO<sub>2</sub> substrate using CVD grown bilayer graphene and gold assisted millimeter-scale exfoliated MoS<sub>2</sub>. We sequentially transferred the 2D layers, used atomic layer deposition (ALD) to grow the HfO<sub>x</sub>, and used photolithography to pattern each layer. Then, we transferred the fabricated 2D S-TFT onto a prestretched elastomer loaded into a strain stage. As shown in Figure S3, we then use the strain stage to systematically release the prestretch, thereby compressing the initially flat S-TFT and inducing wrinkling.

Figures 1b—e show the optical images and schematic cross section of the profile parallel to the channel of the 2D S-TFT (b, c) after transferring onto the prestretched elastomer and (d, e) after releasing the prestretch to the elastomer. As seen in Figures 1b,c, after transferring the 2D S-TFT onto the prestretched elastomer, small wrinkles randomly form on the channel and electrodes. As seen in Figures 1d,e, upon releasing the substrate prestretch, the 2D S-TFT forms wrinkles aligned perpendicular to the strain direction. The compression in the 2D S-TFT is relieved by these out-of-plane wrinkles, which may then be reversibly flattened by restretching.

We employ three different definitions of strain to capture the mechanics at every length scale: (1) Substrate strain ( $\varepsilon_{\text{sub}}$ ) describes the stretchability of the substrate and is important to applications. We define  $\varepsilon_{\rm sub}$  as the change in length of the elastomer over its original length before stretching. (2) TFT strain  $(\varepsilon_{\text{TFT}})$  accounts for the amount of substrate strain that actually gets transmitted into individual devices and is most relevant for understanding the microscale mechanics. We define  $\varepsilon_{\text{TFT}}$  as the change in length of the 2D S-TFT over its original length, induced by the release of prestretch in the elastomer. (3) Intrinsic material strain applies to the MoS<sub>2</sub> channel  $(\varepsilon_{MoS_2})$ , which relates how deformations should affect the electronic properties. In all cases, positive values refer to tensile strain, while negative values refer to compressive strain. Summarized in Figure S3, we analyzed the relationship between  $arepsilon_{
m sub}$  and  $arepsilon_{
m TFT}$  by optically measuring the change in length of both elastomer and 2D S-TFT and found that  $\Delta arepsilon_{ ext{TFT}}$ =  $-0.5\Delta\varepsilon_{\rm sub}$ . Moreover, Figure S4 shows the 2D S-TFT is capable of withstanding compression of  $\varepsilon_{\mathrm{TFT}} > -17\%$  before the supporting HfO<sub>x</sub> thin film starts to fracture, corresponding

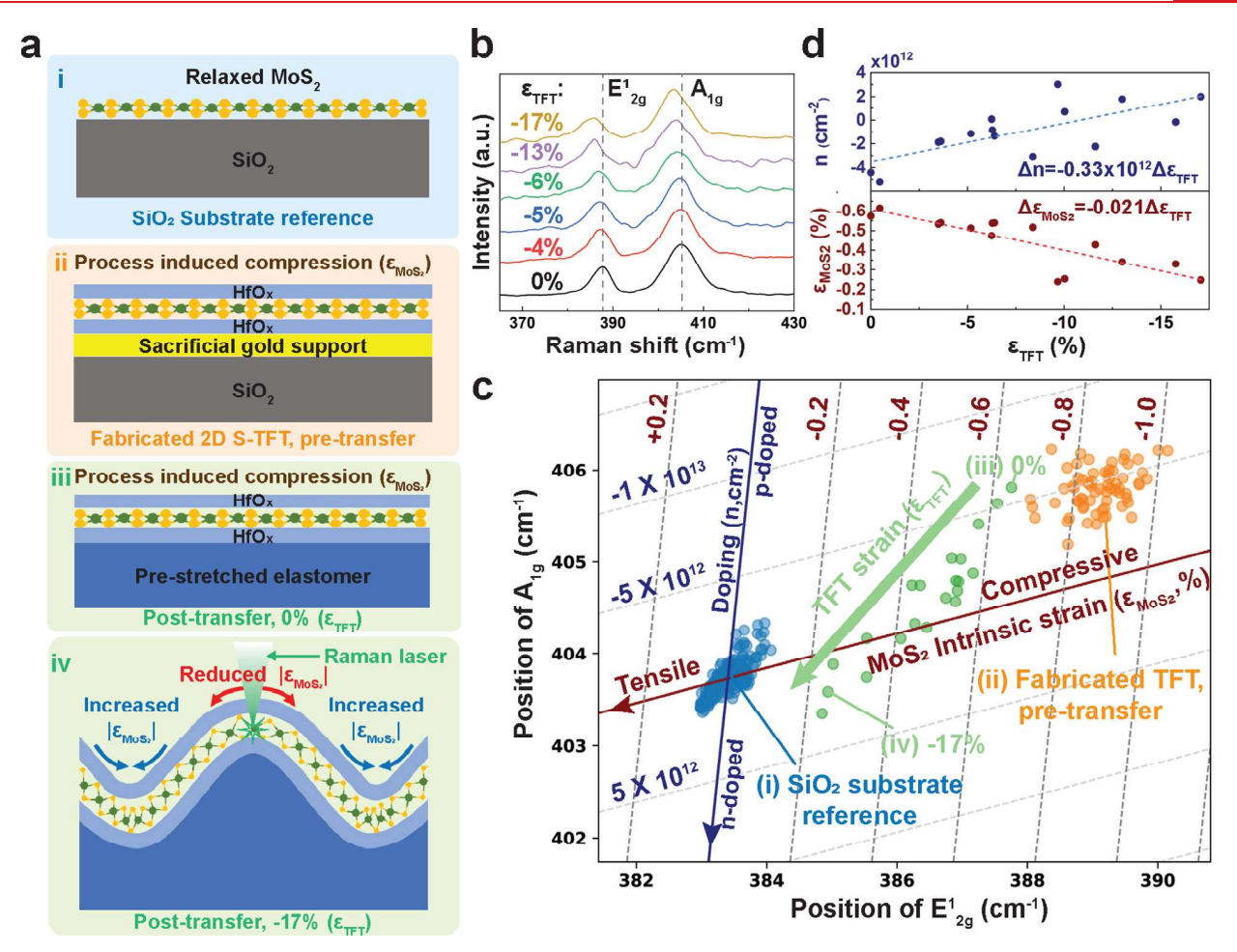


Figure 2. Raman analysis of the strain and doping of 2D S-TFT. (a) Schematic showing the critical stages of fabrication (steps i—iv), with the interpretation of the corresponding strain state. (b) Raman spectra from the crest of a wrinkle in the MoS<sub>2</sub> channel for increasing applied compression  $\varepsilon_{\text{TFT}}$ . The Savitzky—Golay algorithm is used to smooth the Raman spectra. (c) Scatter plot of the  $E_{1g}^1$  and  $A_{1g}$  peak positions. The dashed grid shows the relative strain and doping values. The reference (blue, i) and pretransfer (orange, ii) data sets are from a Raman map spanning the whole channel. The progressively compressed data set (green, iii—iv) is composed of point measurements taken at the same position on the crest of a wrinkle in the channel. (d) Plot of  $\varepsilon_{\text{MoS}_3}$  and  $n_{\text{MoS}_3}$  versus applied  $\varepsilon_{\text{TFT}}$ .

with a prestretch of  $\varepsilon_{\rm sub}$  < 25%. As a result, we kept all measurements below  $\varepsilon_{\rm sub}$  < 25%, a limit defined by the HfO<sub>x</sub> dielectric, not the 2D layers.

Figure 2 explores the impact of wrinkling on the intrinsic strain in the monolayer MoS<sub>2</sub> channel by using micro-Raman spectroscopy. Figure 2a illustrates key stages of fabrication of the 2D S-TFT relevant to the mechanical characterization, along with the interpreted strain state: (i) exfoliated MoS<sub>2</sub> monolayer on SiO<sub>2</sub> substrate, used as a reference; (ii) the MoS<sub>2</sub> monolayer with other active device layers after the 2D S-TFT has been prepatterned on top of the sacrificial gold support layer before transfer; (iii) the flat 2D S-TFT after transfer to the prestretched elastomer substrate; (iv) the wrinkled 2D S-TFT after releasing the prestretch from the elastomer.

Figure 2b plots the Raman spectra of the characteristic  $E_{2g}^{l}$  and  $A_{1g}$  Raman modes of the  $MoS_2$  as the prestretch in the substrate is sequentially released by controlled amounts to induce compression in the 2D S-TFT,  $\varepsilon_{TFT} = 0\%$  and finishing at  $\varepsilon_{TFT} = -17\%$ . We focused the excitation laser spot on the same position on the crest of a central wrinkle to ensure consistent measurements as the morphology changes. The  $E_{2g}^{l}$  and  $A_{1g}$  modes start at 387.2  $\pm$  0.4 and 405.4  $\pm$  0.2 cm<sup>-1</sup> at

 $\varepsilon_{\rm TFT}$  = 0%, respectively, and then shift down under increasing  $\varepsilon_{\rm TFT}.$ 

We quantify the change in strain and doping in the  $MoS_2$  through vector decomposition of the Raman mode shifts. <sup>48,49</sup> Figure 2c shows a scatter plot correlating the relative  $E_{2g}^1$  and  $A_{1g}$  peak positions of the  $MoS_2$  through the 4 steps described in Figure 2a. Both Raman modes are sensitive to both strain  $\varepsilon_{MoS_2}$  and doping  $n_{MoS_2}$ , but shift at different rates, shown in the sheared grid in Figure 2c, allowing us to extract their relative contributions at each step. <sup>48,49</sup> We assumed uniaxial strain and used  $MoS_2$  on  $SiO_2$  (step i, blue) as a reference of the strain and doping. <sup>48,49</sup> Supporting Information Section 1.2 gives the formula and Grüneisen parameters.

After integration into the 2D S-TFT stack on the sacrificial gold transfer layer (step ii, orange), the MoS<sub>2</sub> exhibited a change in compression of  $\Delta \varepsilon_{\text{MoS}_2} = -0.86 \pm 0.06\%$  and an effective p-doping  $\Delta n_{\text{MoS}_2} = -4.5 \times 10^{12}$  cm<sup>-2</sup>. This compression and doping were maintained after transfer onto the prestretched substrate (step iii). Figure 2d plots the change in  $\varepsilon_{\text{MoS}_2}$  and  $n_{\text{MoS}_2}$  at the crest of a wrinkle versus the applied compression  $\varepsilon_{\text{TFT}}$  from 0% (step iii) to -17% (step iv). Only 2% of the change in strain in device  $\varepsilon_{\text{TFT}}$  is transferred into the

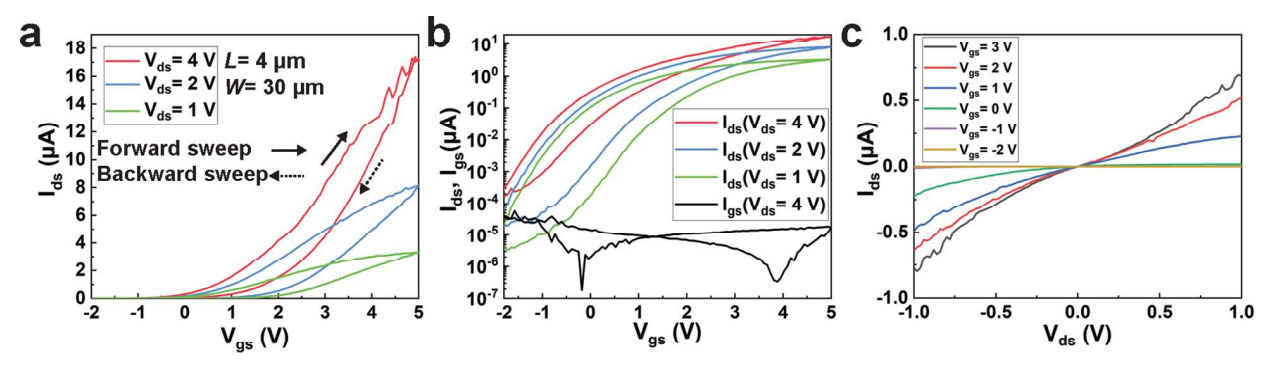


Figure 3. Transfer and output characteristics of a 2D S-TFT before applying any substrate deformation (a) linear and (b) semilog scale of transfer curve with different  $V_{\rm ds}$ . (c) Output curve with different  $V_{\rm gs}$ .

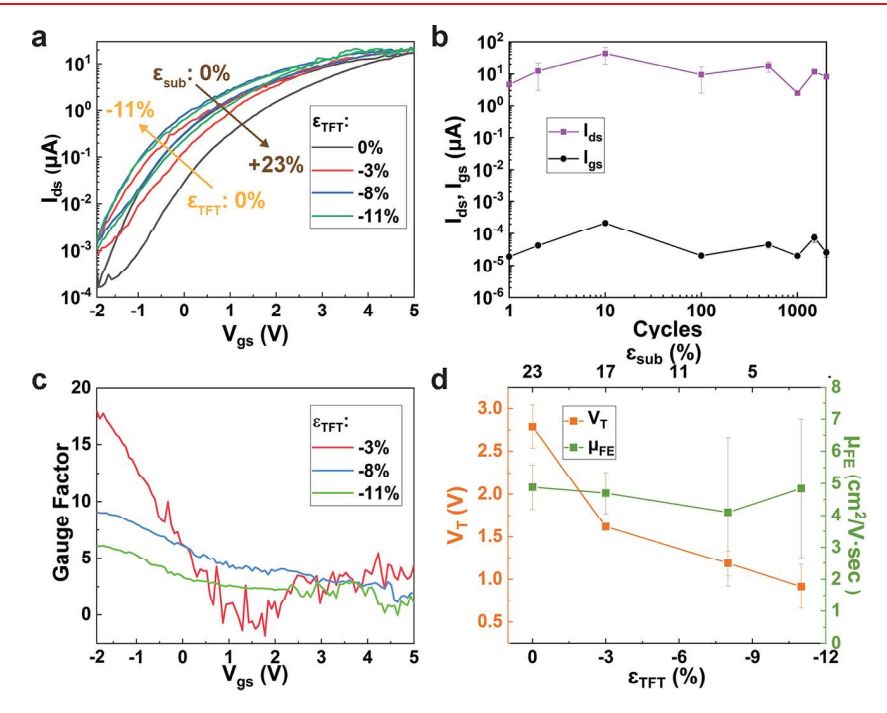


Figure 4. Behavior of the 2D S-TFT under strain. (a) Transfer curve of the 2D S-TFT before and after applying  $\varepsilon_{\rm TFT}$  in semilog scale ( $V_{\rm ds}=4$  V). (b) On-current  $I_{\rm ds}$  and leakage current  $I_{\rm gs}$  of a second 2D S-TFT at  $V_{\rm gs}=6$  V and  $V_{\rm ds}=4$  V over the course of 2000 cycles of stretch between 0% and +23%. (c) Calculated gauge factors of the 2D S-TFT under  $\varepsilon_{\rm TFT}$ . (d)  $V_{\rm T}$  and  $\mu_{\rm FE}$  of the 2D S-TFT under  $\varepsilon_{\rm TFT}$  (top axis shows the corresponding  $\varepsilon_{\rm sub}$ ).

2D channel at the top of the wrinkle. Simultaneously, the compression also impacts the effective doping, causing a shift at a rate of 0.33  $\times$  10<sup>12</sup> cm<sup>-2</sup>/%, from  $n_{MoS}$ , = (-5  $\pm$  0.9)  $\times$  $10^{12}$  cm<sup>-2</sup> (p-type) at  $\varepsilon_{\rm TFT}$  = 0% to  $n_{\rm MoS_2}$  = (2.5  $\pm$  0.8)  $\times$  10<sup>12</sup> cm<sup>-2</sup> (n-type) at  $\varepsilon_{\rm TFT}$  = -17%. We interpret the initial compression in the MoS<sub>2</sub> to be from process-induced strains, which could be induced by the deposition of the HfO<sub>x</sub> film,<sup>50</sup> or transfer process. 51,52 The shift of  $\varepsilon_{MoS_2}$  as the stretch in the substrate is released indicates a reduction of the compressive strain. In Figures S5 and S6, we perform additional Raman and photoluminescence (PL) analysis on wrinkled thin films under compression, which show that the measured trend is consistent with previous results on 2D materials on thin films under compression, where wrinkling induces periodic modulation in strain with tensile strain at the crest of the wrinkle and compressive strain at the trough of the wrinkle. 31,32,53,54

Taken together, both Raman and PL analyses revealed that wrinkling reduced the magnitude of strain received by the

MoS<sub>2</sub> by more than a factor of 50 compared with the strain being applied to the 2D S-TFT. This allows the 2D S-TFT to withstand much larger substrate deformations than would normally be allowed by the fracture strain of the MoS<sub>2</sub> of 11%.<sup>55</sup> We hypothesize that the strain induced n-doping can be caused by tuning of the conduction band edge relative to the Fermi level,<sup>56,57</sup> which we will investigate further through transport characteristics of the 2D S-TFT.

Figure 3 investigates the electrical transport behavior in the stretchable 2D S-TFT in the prerelease flat state. Figures 3a and 3b plot the transfer characteristics of the 2D S-TFT under different drain—source biases ( $V_{\rm ds}$ ) in linear and semilog scales, respectively. The 2D S-TFT demonstrate n-type behavior, consistent with the behavior of graphene-contacted MoS<sub>2</sub> transistors. We note that these devices did not reach the saturation regime due to the dielectric breakdown for  $V_{\rm ds}-V_{\rm gs}>6$  V. Figure 3c plots the output characteristic of the 2D S-TFT for different  $V_{\rm gs}$  from -2 to 3 V. The output curves show a symmetric linear relationship between  $I_{\rm ds}$  and  $V_{\rm ds}$ , indicating

Table 1. Benchmark Data of Stretchability and Mobility for Various MoS<sub>2</sub> Transistors Have Been Reported in the Literature

channel material (no. of layers)	type of deformation	channel contact/dielectric/gate electrode	stretchability (%)	mobility $(cm^2/(V s))$	ref
MoS <sub>2</sub> (2 L)	stretching	graphene/HfO <sub>x</sub> /graphene	23	4.9	this work
$MoS_2$ (1 L)	stretching	Au/hBN/Au	14	30	44
$MoS_2$ (4 L)	stretching	Au/EDL <sup>a</sup> /ionic liquid	8	3.39	28
$MoS_2$ (3 L)	stretching	Au/ion-gel/Au	5	1.4	43
$MoS_2$ (1 L)	stretching	graphene/Al <sub>2</sub> O <sub>3</sub> /Pd	4	0.56	45
$MoS_2$ (1 L)	bending	Au/Al <sub>2</sub> O <sub>3</sub> /Au	2.1	55	20
$MoS_2$ (3 L)	bending	Au/hBN/Au	1.5	45	23
$MoS_2$ (1 L)	bending	Au/Al <sub>2</sub> O <sub>3</sub> /Au	0.7	10.8	22
$MoS_2$ (1 L)	bending	graphene/hBN/graphene	0.17	21	60
$MoS_2$ (2 L)	bending	$Au/Al_2O_3/Au$	0.08	16.2	24

<sup>a</sup>EDL: electrical double layers.

low Schottky barriers. We extracted the critical performance metrics for thin film transistors: threshold voltage  $V_{\rm T}=2.8\pm0.3$  V, subthreshold swing SS = 440  $\pm$  36 mV/dec, on/off ratio  $I_{\rm on/off}=10^{\rm S}$ , and field effect mobility  $\mu_{\rm FE}=4.9\pm0.7$  cm²/(V s). Figure 4 explores how strain and wrinkling impact the electrical performance of 2D S-TFT. Figure 4a (and Figure S7)

Figure 4 explores how strain and wrinkling impact the electrical performance of 2D S-TFT. Figure 4a (and Figure S7) plot the transfer characteristic of the 2D S-TFT under different levels of applied strain  $\varepsilon_{\mathrm{TFT}}$  from 0% to -11% (corresponding with a substrate stretch from +23% to 0%) in semilog scale and linear scale, respectively. Through the entire strain range, the ON-current maintains a value of  $I_{ds} \sim 10 \mu A$  at  $V_{gs} = 5 \text{ V}$ . Meanwhile, as shown in Figure S7, the leakage current  $(I_{gs})$ remains less than 100 pA over the entire strain range, which indicates that the gate dielectric is effectively resistant to pinholes under wrinkling. To demonstrate the reversibility of the wrinkling process, Figure 4b plots the on-current of  $I_{ds}$  and  $I_{\rm gs}$  of a new device under repeated cycling of stretching and releasing  $\varepsilon_{\rm sub}$  from 0% to +23%, measured at  $V_{\rm gs}$  = 6 V and  $V_{\rm ds}$ = 4 V. Over the course of the 2000 cycles, the on-current of  $I_{\rm ds}$ remained over  $10^{-6}$  A while  $I_{\rm gs}$  remained under  $3 \times 10^{-10}$  Å, indicating that the 2D S-TFT channel and gate dielectric maintain electrical integrity of both the gate and channel without degradation under repeated strain cycles.

Next we quantify how  $\varepsilon_{\rm TFT}$  modifies the electrical performance of 2D S-TFT. Figure 4c plots the gauge factor versus gate under different levels of  $\varepsilon_{\rm TFT}$ . The gauge factor is determined by the formula  $(R_{\rm s}-R_{\rm 0})/(\varepsilon_{\rm TFT}R_{\rm 0})$ , where  $R_{\rm s}$  is the resistance with applied  $\varepsilon_{\rm TFT}$  and  $R_{\rm 0}$  is the initial resistance at  $\varepsilon_{\rm TFT}=0\%$ . Under varying  $\varepsilon_{\rm TFT}$ , the gauge factor consistently falls within the range of -1.8 to +17.9, with the largest gauge factors occurring at negative gate biases, when the 2D S-TFT is near the off state. Notably, the gauge factor is considerably lower than the reported values for flexible MoS $_2$  transistors under bending strain, which range from 200 to 575294 under ranging from -0.2% to +0.7% intrinsic strain.  $^{22,59,60}$ 

Figure 4d shows the extracted  $\mu_{\rm FE}$  and  $V_{\rm T}$  values under different levels of  $\varepsilon_{\rm TFT}$ . Table S1 provides the corresponding extracted values of  $\mu_{\rm FE}$ ,  $V_{\rm T}$ , as well as SS, and  $I_{\rm on/off}$  for different  $\varepsilon_{\rm TFT}$ . Most significantly,  $V_{\rm T}$  decreases by  $\Delta V_{\rm T} = -1.9$  V (out of 8 V in the full measurement range) at  $\varepsilon_{\rm TFT} = -11\%$ . Meanwhile, the  $\mu_{\rm FE}$  does not significantly change under compression, with a maximum reduction of only 0.8 cm²/(V s) at -8%  $\varepsilon_{\rm TFT}$ , smaller than the variability in the measurement. Similarly, the SS starts at a value of  $436\pm36$  mV/dec, and just like mobility, it exhibits only slight changes under  $\varepsilon_{\rm TFT}$  of up to -49 mV/dec relative to  $\varepsilon_{\rm TFT} = 0\%$ . Finally, the  $I_{\rm on/off}$  starts at  $1.5\times10^{5}$  and decreases by approximately a factor of 3 to  $4.5\times10^{4}$  under increasing  $\varepsilon_{\rm TFT}$ .

Taken together,  $\mu_{\rm FE}$  and SS do not meaningfully change as a function of strain. The observed shift in  $\Delta V_{\rm T} = -1.9$  V through transport measurements are consistent with the shift that would result from a strain induced change in doping observed in the Raman analysis, which predict a shift of  $\Delta V_{\rm T} = -1.5$  V (see the Supporting Information Section 1.2). The primary change in all other factors may be explained by the shift in  $V_{\rm T}$ , which corresponds to a shift in the transfer curve to negative gate bias. The resulting increase in conductivity leads to the largest values of gauge factor. Similarly, the effective reduction in  $I_{\rm on/off}$  is a result of the shift of the off state beyond the gate range accessible without inducing breakdown. We hypothesize that if the gate dielectrics could withstand larger voltages before breakdown, then the  $I_{\rm on/off}$  would not significantly change.

Other studies on strain engineering 2D materials offers insights into the possible reasons for the  $V_{\rm T}$  shift. For example, MoS<sub>2</sub> transistors under strain through techniques like substrate bending show shifts in the  $V_{\rm T}$  in the range of 1 V at up to +0.7% strain with a 20 nm thick Al<sub>2</sub>O<sub>3</sub> dielectric layer. <sup>22</sup> These shifts are comparable to the values measured here and the changes in intrinsic strains from wrinkling observed in Figure 2. We attribute the shifts in  $V_{\rm T}$  to increasing electron density with a decreasing band gap under increasing tensile strain. However, the samples measured here should have heterogeneous strain due to the wrinkling (Figure S5) and thus heterogeneity in the local conductivity. In that regard, it is surprising that the results show a trend consistent with strain engineering in flat devices.

Finally, Table 1 benchmarks the performance of the 2D S-TFT reported here by comparing the stretchability and  $\mu_{\rm FE}$  with the demonstrations in the literature. This table shows that 2D S-TFT demonstrated here are comparable to the state of the art of stretchable transistors with the highest stretchability (23%). The mobility (4.9  $\pm$  0.7 cm²/(V s)) is not the highest measured but is respectable, even by the standards of 2D electronics on hard substrates. There is still significant room for improvement if the additional challenges of bringing the devices onto soft substrates could be overcome. For example, effective removal of processing residue is a challenge when integrating with soft substrates, which can affect accurate capacitance estimates, hysteresis, and dielectric breakdown (see the Supporting Information and Figure S8).

This study introduces a pioneering strategy for the heterogeneous integration of 2D, soft, and CMOS thin films that lays the foundation for the development of new kinds of stretchable logic gates and integrated circuits crucial for flexible and stretchable electronic applications that require signal

processing and computation. Furthermore, these results build a fundamental understanding of the impact of heterogeneous strain on the electron transport of 2D semiconductors. In this study, we demonstrated the development of an S-TFT with wrinkled 2D heterostructures. The integration of buckling engineering, kirigami patterning, and the unique bending properties of 2D materials offers a novel approach for designing stretchable TFTs, which effectively mitigates the mechanical fracture of traditionally brittle components, such as metal electrodes, under large strain and wrinkling. By incorporating stacked 2D materials in the S-TFT, we have leveraged the practical application of a low friction 2D interface at the device level. An ongoing challenge is that the failure point under strain appears to occur within the ALD dielectric layers. This implies that further stretchability could be achieved by substituting these remaining layers with another 2D dielectric material, like h-BN. Looking ahead, while this work has focused on single devices from MoS2, the fabrication strategies are fully scalable and agnostic to the specific material. As such, they could be applied to any 2D material-based transistors<sup>61</sup> and also be applied to technologies.

### ASSOCIATED CONTENT

### **Data Availability Statement**

The data of this study may be accessed in the Illinois Data Bank repository, 10.13012/B2IDB-7325893 V1.

# Supporting Information

The Supporting Information is available free of charge at https://pubs.acs.org/doi/10.1021/acs.nanolett.3c05091.

Figures S1–S8; (Section 1.1) methods, (Section 1.2.1) vector decomposition of  $MoS_2$  Raman peak positions, (Section 1.2.2) capacitance and mobility calculation for the 2D S-TFT, and (Section 1.2.3) predicted threshold shift from strain-induced doping (PDF)

### AUTHOR INFORMATION

### **Corresponding Author**

Arend M. van der Zande — Department of Mechanical Science and Engineering, University of Illinois Urbana—Champaign, Urbana, Illinois 61801, United States; Materials Research Lab, Materials Science and Engineering, and Holonyak Micro and Nano Technology Lab, University of Illinois Urbana—Champaign, Urbana, Illinois 61801, United States; orcid.org/0000-0001-5104-9646; Email: arendv@illinois.edu

## **Authors**

Hyunchul Kim — Department of Mechanical Science and Engineering, University of Illinois Urbana—Champaign, Urbana, Illinois 61801, United States; ⊙ orcid.org/0000-0002-6883-6985

**He Lin Zhao** — Department of Electrical and Computer Engineering, University of Illinois Urbana—Champaign, Urbana, Illinois 61801, United States

Complete contact information is available at: https://pubs.acs.org/10.1021/acs.nanolett.3c05091

# **Author Contributions**

All authors conceived the experiments, contributed to interpretation, and wrote the manuscript. H.K. and H.Z performed sample fabrication. H.Z. performed Raman experi-

ments and analysis. H.K. performed transport experiments and analysis. A.M.v.d.Z. supervised all activities.

#### Notes

The authors declare no competing financial interest.

#### ACKNOWLEDGMENTS

This work was entirely supported by supported by the NSF through the University of Illinois at Urbana—Champaign Materials Research Science and Engineering Center under Awards DMR-1720633 and DMR-2309037. This work was performed in part in the Holonyak Micro and Nano Technology Laboratory (HMNTL) and the Materials Research Laboratory Central Facilities (MRL), all at the University of Illinois. The authors acknowledge the use of facilities and instrumentation supported by NSF through the University of Illinois Materials Research Science and Engineering Center DMR-2309037.

# REFERENCES

- (1) Kaltenbrunner, M.; Sekitani, T.; Reeder, J.; Yokota, T.; Kuribara, K.; Tokuhara, T.; Drack, M.; Schwödiauer, R.; Graz, I.; Bauer-Gogonea, S.; Bauer, S.; Someya, T. An ultra-lightweight design for imperceptible plastic electronics. *Nature* **2013**, *499*, 458–463.
- (2) Liu, Y.; Pharr, M.; Salvatore, G. A. Lab-on-skin: a review of flexible and stretchable electronics for wearable health monitoring. *ACS Nano* **2017**, *11*, 9614–9635.
- (3) Van Den Brand, J.; de Kok, M.; Koetse, M.; Cauwe, M.; Verplancke, R.; Bossuyt, F.; Jablonski, M.; Vanfleteren, J. Flexible and stretchable electronics for wearable health devices. *Solid-State Electron.* **2015**, *113*, 116–120.
- (4) Wang, S.; et al. Skin electronics from scalable fabrication of an intrinsically stretchable transistor array. *Nature* **2018**, 555, 83–88.
- (5) Kim, J.; et al. Stretchable silicon nanoribbon electronics for skin prosthesis. *Nat. Commun.* **2014**, *5*, 5747.
- (6) Kim, K. K.; Suh, Y.; Ko, S. H. Smart stretchable electronics for advanced human—machine interface. *Adv. Intell. Syst* **2021**, 3, 2000157
- (7) Dai, Y.; Hu, H.; Wang, M.; Xu, J.; Wang, S. Stretchable transistors and functional circuits for human-integrated electronics. *Nat. Electron.* **2021**, *4*, 17–29.
- (8) Wang, M.; Wang, T.; Luo, Y.; He, K.; Pan, L.; Li, Z.; Cui, Z.; Liu, Z.; Tu, J.; Chen, X. Fusing stretchable sensing technology with machine learning for human—machine interfaces. *Adv. Funct. Mater.* **2021**, *31*, 2008807.
- (9) Byun, J.; Lee, Y.; Yoon, J.; Lee, B.; Oh, E.; Chung, S.; Lee, T.; Cho, K.-J.; Kim, J.; Hong, Y. Electronic skins for soft, compact, reversible assembly of wirelessly activated fully soft robots. *Sci. Robot.* **2018**, *3*, No. eaas9020.
- (10) Cacucciolo, V.; Shintake, J.; Kuwajima, Y.; Maeda, S.; Floreano, D.; Shea, H. Stretchable pumps for soft machines. *Nature* **2019**, *572*, 516–519.
- (11) Van Der Zande, A.; Hone, J. Inspired by strain. *Nat. Photonics* **2012**, *6*, 804–806.
- (12) Wu, F.; Liu, Y.; Zhang, J.; Duan, S.; Ji, D.; Yang, H. Recent Advances in High-Mobility and High-Stretchability Organic Field-Effect Transistors: From Materials, Devices to Applications. *Small Methods* **2021**, *5*, 2100676.
- (13) Cao, K.; Feng, S.; Han, Y.; Gao, L.; Ly, T. H.; Xu, Z.; Lu, Y. Elastic straining of free-standing monolayer graphene. *Nat. Commun.* **2020**, *11*, 1–7.
- (14) Yu, J.; Hossain, M. A.; Kim, S.; Ferrari, P. F.; Huang, S.; Zhang, Y.; Kim, H.; Michel, D. A.; van der Zande, A. M. Mechanically sensing and tailoring electronic properties in two-dimensional atomic membranes. *Curr. Opin. Solid State Mater. Sci.* **2021**, 25, 100900.
- (15) Akinwande, D.; Petrone, N.; Hone, J. Two-dimensional flexible nanoelectronics. *Nat. Commun.* **2014**, *5*, 5678.

- (16) Hoang, A. T.; Hu, L.; Katiyar, A. K.; Ahn, J.-H. Two-dimensional layered materials and heterostructures for flexible electronics. *Matter* **2022**, *5*, 4116–4132.
- (17) Choi, M.; Bae, S.-R.; Hu, L.; Hoang, A. T.; Kim, S. Y.; Ahn, J.-H. Full-color active-matrix organic light-emitting diode display on human skin based on a large-area MoS2 backplane. *Sci. Adv.* **2020**, *6*, No. eabb5898.
- (18) Choi, C.; Leem, J.; Kim, M.; Taqieddin, A.; Cho, C.; Cho, K. W.; Lee, G. J.; Seung, H.; Bae, H. J.; Song, Y. M.; Hyeon, T.; Aluru, N. R.; Nam, S.; Kim, D.-H. Curved neuromorphic image sensor array using a MoS2-organic heterostructure inspired by the human visual recognition system. *Nat. Commun.* **2020**, *11*, 5934.
- (19) Kireev, D.; Sel, K.; Ibrahim, B.; Kumar, N.; Akbari, A.; Jafari, R.; Akinwande, D. Continuous cuffless monitoring of arterial blood pressure via graphene bioimpedance tattoos. *Nat. Nanotechnol.* **2022**, *17*, 864–870.
- (20) Li, N.; Wang, Q.; Shen, C.; Wei, Z.; Yu, H.; Zhao, J.; Lu, X.; Wang, G.; He, C.; Xie, L.; Zhu, J.; Du, L.; Yang, R.; Shi, D.; Zhang, G. Large-scale flexible and transparent electronics based on monolayer molybdenum disulfide field-effect transistors. *Nat. Electron.* **2020**, *3*, 711–717.
- (21) Tang, J.; et al. Low power flexible monolayer MoS2 integrated circuits. *Nat. Commun.* **2023**, *14*, 3633.
- (22) Datye, I. M.; Daus, A.; Grady, R. W.; Brenner, K.; Vaziri, S.; Pop, E. Strain-Enhanced Mobility of Monolayer MoS2. *Nano Lett.* **2022**, 22, 8052–8059.
- (23) Lee, G.-H.; Yu, Y.-J.; Cui, X.; Petrone, N.; Lee, C.-H.; Choi, M. S.; Lee, D.-Y.; Lee, C.; Yoo, W. J.; Watanabe, K.; Taniguchi, T.; Nuckolls, C.; Kim, P.; Hone, J. Flexible and transparent MoS2 field-effect transistors on hexagonal boron nitride-graphene heterostructures. *ACS Nano* **2013**, *7*, 7931–7936.
- (24) Park, Y. J.; Sharma, B. K.; Shinde, S. M.; Kim, M.-S.; Jang, B.; Kim, J.-H.; Ahn, J.-H. All MoS2-based large area, skin-attachable active-matrix tactile sensor. *ACS Nano* **2019**, *13*, 3023–3030.
- (25) Zang, J.; Ryu, S.; Pugno, N.; Wang, Q.; Tu, Q.; Buehler, M. J.; Zhao, X. Multifunctionality and control of the crumpling and unfolding of large-area graphene. *Nat. Mater.* **2013**, *12*, 321–325.
- (26) Kim, M.; Kang, P.; Leem, J.; Nam, S. A stretchable crumpled graphene photodetector with plasmonically enhanced photoresponsivity. *Nanoscale* **2017**, *9*, 4058–4065.
- (27) Hossain, M. A.; Yu, J.; van der Zande, A. M. Realizing optoelectronic devices from crumpled two-dimensional material heterostructures. *ACS Appl. Mater. Interfaces.* **2020**, *12*, 48910–48916.
- (28) Park, S.; Song, J.; Kim, T. K.; Choi, K.-H.; Hyeong, S.-K.; Ahn, M.; Kim, H. R.; Bae, S.; Lee, S.-K.; Hong, B. H. Photothermally Crumpled MoS2 Film as an Omnidirectionally Stretchable Platform. *Small Methods* **2022**, *6*, 2200116.
- (29) Kang, P.; Wang, M. C.; Knapp, P. M.; Nam, S. Crumpled graphene photodetector with enhanced, strain-tunable, and wavelength-selective photoresponsivity. *Adv. Mater.* **2016**, 28, 4639–4645.
- (30) Rhee, D.; Paci, J. T.; Deng, S.; Lee, W.-K.; Schatz, G. C.; Odom, T. W. Soft skin layers enable area-specific, multiscale graphene wrinkles with switchable orientations. ACS Nano 2020, 14, 166–174.
- (31) Lee, J.; Yun, S. J.; Seo, C.; Cho, K.; Kim, T. S.; An, G. H.; Kang, K.; Lee, H. S.; Kim, J. Switchable, tunable, and directable exciton funneling in periodically wrinkled WS2. *Nano Lett.* **2021**, *21*, 43–50.
- (32) Hossain, M. A.; Zhang, Y.; van der Zande, A. M. Strain engineering photonic properties in monolayer semiconductors through mechanically-reconfigurable wrinkling. Physical Chemistry of Semiconductor Materials and Interfaces XIX. *Proceedings of SPIE* **2020**, 1146404.
- (33) Blees, M. K.; Barnard, A. W.; Rose, P. A.; Roberts, S. P.; McGill, K. L.; Huang, P. Y.; Ruyack, A. R.; Kevek, J. W.; Kobrin, B.; Muller, D. A.; McEuen, P. L. Graphene kirigami. *Nature* **2015**, *524*, 204–207.
- (34) Yong, K.; De, S.; Hsieh, E. Y.; Leem, J.; Aluru, N. R.; Nam, S. Kirigami-inspired strain-insensitive sensors based on atomically-thin materials. *Mater. Today* **2020**, *34*, 58–65.
- (35) Li, Z.; et al. Efficient strain modulation of 2D materials via polymer encapsulation. *Nat. Commun.* **2020**, *11*, 1151.

- (36) Li, Z.; Chen, Y.; Liu, S.; Li, W.; Liu, L.; Song, W.; Lu, D.; Ma, L.; Yang, X.; Xie, Z.; Duan, X.; Yang, Z.; Wang, Y.; Liao, L.; Liu, Y. Strain Releasing of Flexible 2D Electronics through van der Waals Sliding Contact. ACS Nano 2022, 16, 13152–13159.
- (37) Han, E.; Yu, J.; Annevelink, E.; Son, J.; Kang, D. A.; Watanabe, K.; Taniguchi, T.; Ertekin, E.; Huang, P. Y.; van der Zande, A. M. Ultrasoft slip-mediated bending in few-layer graphene. *Nat. Mater.* **2020**, *19*, 305–309.
- (38) Yu, J.; Han, E.; Hossain, M. A.; Watanabe, K.; Taniguchi, T.; Ertekin, E.; van der Zande, A. M.; Huang, P. Y. Designing the bending stiffness of 2D material heterostructures. *Adv. Mater.* **2021**, *33*, 2007269.
- (39) Kim, J.; Leem, J.; Kim, H. N.; Kang, P.; Choi, J.; Haque, M. F.; Kang, D.; Nam, S. Uniaxially crumpled graphene as a platform for guided myotube formation. *Microsyst. Nanoeng.* **2019**, *5*, 53.
- (40) Park, M.; Park, Y. J.; Chen, X.; Park, Y.-K.; Kim, M.-S.; Ahn, J.-H. MoS2-based tactile sensor for electronic skin applications. *Adv. Mater.* **2016**, 28, 2556–2562.
- (41) Zhang, W.; Liu, Y.; Pei, X.; Yuan, Z.; Zhang, Y.; Zhao, Z.; Hao, H.; Long, R.; Liu, N. Stretchable MoS2 Artificial Photoreceptors for E-Skin. *Adv. Funct. Mater.* **2022**, *32*, 2107524.
- (42) Fu, X.-W.; Liao, Z.-M.; Zhou, J.-X.; Zhou, Y.-B.; Wu, H.-C.; Zhang, R.; Jing, G.; Xu, J.; Wu, X.; Guo, W.; Yu, D. Strain dependent resistance in chemical vapor deposition grown graphene. *Appl. Phys. Lett.* **2011**, *99*, 213107.
- (43) Pu, J.; Zhang, Y.; Wada, Y.; Tse-Wei Wang, J.; Li, L.-J.; Iwasa, Y.; Takenobu, T. Fabrication of stretchable MoS2 thin-film transistors using elastic ion-gel gate dielectrics. *Appl. Phys. Lett.* **2013**, *103*, 023505.
- (44) Li, J.; Li, N.; Wang, Q.; Wei, Z.; He, C.; Shang, D.; Guo, Y.; Zhang, W.; Tang, J.; Liu, J.; Wang, S.; Yang, W.; Yang, R.; Shi, D.; Zhang, G. Highly Stretchable MoS2-Based Transistors with Opto-Synaptic Functionalities. *Adv. Electron. Mater.* **2022**, *8*, 2200238.
- (45) Park, I.-J.; Kim, T. I.; Kang, S.; Shim, G. W.; Woo, Y.; Kim, T.-S.; Choi, S.-Y. Stretchable thin-film transistors with molybdenum disulfide channels and graphene electrodes. *Nanoscale* **2018**, *10*, 16069–16078.
- (46) Yan, Z.; Xu, D.; Lin, Z.; Wang, P.; Cao, B.; Ren, H.; Song, F.; Wan, C.; Wang, L.; Zhou, J.; Zhao, X.; Chen, J.; Huang, Y.; Duan, X. Highly stretchable van der Waals thin films for adaptable and breathable electronic membranes. *Science* **2022**, *375*, 852–859.
- (47) Ruiz-Vargas, C. S.; Zhuang, H. L.; Huang, P. Y.; Van Der Zande, A. M.; Garg, S.; McEuen, P. L.; Muller, D. A.; Hennig, R. G.; Park, J. Softened elastic response and unzipping in chemical vapor deposition graphene membranes. *Nano Lett.* **2011**, *11*, 2259–2263.
- (48) Michail, A.; Delikoukos, N.; Parthenios, J.; Galiotis, C.; Papagelis, K. Optical detection of strain and doping inhomogeneities in single layer MoS2. *Appl. Phys. Lett.* **2016**, *108*, 173102.
- (49) Kukucska, G.; Koltai, J. Theoretical Investigation of Strain and Doping on the Raman Spectra of Monolayer MoS2. *Phys. Status Solidi B* **2017**, 254, 1700184.
- (50) Peña, T.; Chowdhury, S. A.; Azizimanesh, A.; Sewaket, A.; Askari, H.; Wu, S. M. Strain engineering 2D MoS2 with thin film stress capping layers. 2D Mater. 2021, 8, 045001.
- (51) Velický, M.; Rodriguez, A.; Bouša, M.; Krayev, A. V.; Vondráček, M.; Honolka, J.; Ahmadi, M.; Donnelly, G. E.; Huang, F.; Abrunã, H. D.; Novoselov, K. S.; Frank, O. Strain and Charge Doping Fingerprints of the Strong Interaction between Monolayer MoS2and Gold. *J. Phys. Chem. Lett.* **2020**, *11*, 6112–6118.
- (52) Lee, J.; Wang, Z.; Xie, H.; Mak, K. F.; Shan, J. Valley magnetoelectricity in single-layer MoS2. *Nat. Mater.* **2017**, *16*, 887–891
- (53) Cho, C.; Wong, J.; Taqieddin, A.; Biswas, S.; Aluru, N. R.; Nam, S.; Atwater, H. A. Highly strain-tunable interlayer excitons in MoS2/WSe2 heterobilayers. *Nano Lett.* **2021**, *21*, 3956–3964.
- (54) Quereda, J.; San-Jose, P.; Parente, V.; Vaquero-Garzon, L.; Molina-Mendoza, A. J.; Agraït, N.; Rubio-Bollinger, G.; Guinea, F.; Roldán, R.; Castellanos-Gomez, A. Strong modulation of optical

properties in black phosphorus through strain-engineered rippling. *Nano Lett.* **2016**, *16*, 2931–2937.

- (55) Bertolazzi, S.; Brivio, J.; Kis, A. Stretching and breaking of ultrathin MoS2. ACS Nano 2011, 5, 9703–9709.
- (56) Manzeli, S.; Allain, A.; Ghadimi, A.; Kis, A. Piezoresistivity and strain-induced band gap tuning in atomically thin MoS2. *Nano Lett.* **2015**, *15*, 5330–5335.
- (57) Harats, M. G.; Kirchhof, J. N.; Qiao, M.; Greben, K.; Bolotin, K. I. Dynamics and efficient conversion of excitons to trions in non-uniformly strained monolayer WS2. *Nat. Photonics* **2020**, *14*, 324–329.
- (58) Roy, T.; Tosun, M.; Kang, J. S.; Sachid, A. B.; Desai, S. B.; Hettick, M.; Hu, C. C.; Javey, A. Field-effect transistors built from all two-dimensional material components. *ACS Nano* **2014**, *8*, 6259–6264.
- (59) Zhao, J.; Wei, Z.; Zhang, Q.; Yu, H.; Wang, S.; Yang, X.; Gao, G.; Qin, S.; Zhang, G.; Sun, Q.; Wang, Z. L. Static and dynamic piezopotential modulation in piezo-electret gated MoS2 field-effect transistor. *ACS Nano* **2019**, *13*, 582–590.
- (60) Lee, I.; Kang, W. T.; Shin, Y. S.; Kim, Y. R.; Won, U. Y.; Kim, K.; Duong, D. L.; Lee, K.; Heo, J.; Lee, Y. H.; Yu, W. J. Ultrahigh gauge factor in graphene/MoS2 heterojunction field effect transistor with variable Schottky barrier. *ACS Nano* **2019**, *13*, 8392–8400.
- (61) Zhu, W.; Park, S.; Yogeesh, M. N.; McNicholas, K. M.; Bank, S. R.; Akinwande, D. Black phosphorus flexible thin film transistors at gighertz frequencies. *Nano Lett.* **2016**, *16*, 2301–2306.